A fault surface exposed on Mercury

D. L. Pegg, D. A. Rothery, Susan J. Conway, M. R. Balme

Planetary and Space Science 201 (2021) 105223

Contents lists available at ScienceDirect

Planetary and Space Science

journal homepage: www.elsevier.com/locate/pss

A fault surface exposed on Mercury

D.L. Pegg [a,*], D.A. Rothery [a], S.J. Conway [b], M.R. Balme [a]

[a] The Open University, Milton Keynes, MK7 6AA, UK
[b] CNRS UMR 6112 Laboratoire de Planétologie et Géodynamique, Université de Nantes, France

ARTICLE INFO

Keywords:
Mercury
Tectonics
Fault
Lobate scarp
Vent

ABSTRACT

Mercury's tectonic history has been dominated by global contraction as the planet shrinks and cools. Previously, fault dips have been indirectly estimated by measuring offsets to the rims of craters displaced by fault movement. Here we present the first observations of a fault surface exposed in three dimensions, in this case within a volcanic vent. We use shadow measurements to determine the depth of the vent and have measured the dip of the fault as 28° ±5. This is towards the shallower end of previous dip estimates used to estimate global contraction. If it is representative, it suggests global contraction at the higher end (5.7–7.1 km) of previously published estimates.

1. Introduction

Tectonic and volcanic processes have shaped Mercury's surface over its geological history (Strom et al., 1975; Head et al., 2008, 2009; Watters et al., 2015). Tectonism is manifest in shortening landforms such as lobate scarps, wrinkle ridges, and high relief ridges, which are the dominant surface expression of the planet's global contraction (Dzurisin, 1978; Melosh and McKinnon, 1988; Watters et al., 2009).

A lobate scarp is an asymmetrical ridge that is the surface expression of a thrust fault. They are known to be up to 2 km high on Mercury (Strom et al., 1975; Watters and Nimmo, 2010; Massironi et al., 2015). Wrinkle ridges have a similar surface expression to lobate scarps, but tend to be smaller and more symmetrical (Strom et al., 1975; Watters and Nimmo, 2010; Korteniemi et al., 2015). High relief ridges are broad, symmetrical topographic features, interpreted as high angle reverse faults (Dzurisin, 1978). Initially thought to be a distinct tectonic landforms, subsequent observations show high relief ridges can often transition into lobate scarps and thus are part of a continuum of landforms (Melosh and McKinnon, 1988; Watters et al., 2009; Byrne et al., 2014; Massironi and Byrne, 2015).

Key terminology related to faults in this manuscript includes: the fault plane, which is the surface separating the blocks and along which movement has occurred; strike, the azimuth at which the fault plane intersects the horizontal; and the dip, the angle at which the fault plane descends below the horizontal (Neuendorf et al., 2005).

The stresses in Mercury's crust that have generated this contractional tectonism have multiple possible origins, including global contraction (Watters and Nimmo, 2010), tidal despinning (e.g. Melosh and Dzurisin, 1978), true polar wander (Matsuyama and Nimmo, 2009), and mantle convection (King, 2008). Some of the faulting is localised at the junction between regional geochemical terrains (Galluzzi et al., 2019), or at the edges of smooth plains confined within impact basins (Fegan et al., 2017). Although a combination of factors probably influences many of the visible faults, the dominant cause of contractional tectonics on Mercury is widely accepted to be global contraction of the planet (Klimczak et al., 2015). Mercury's relatively high ratio of surface area to volume means that it has undergone significant cooling, which has led to shrinking (Watters and Nimmo, 2010). Thermal and compositional models of the planet provide a wide range of estimated shrinking; the planet could have shrunk by between 0.6 and 10 km radially (Solomon, 1977; Watters and Nimmo, 2010; Grott et al., 2011).

Byrne et al. (2014) calculated Mercury's global contraction from a global inventory of contractional features combined with estimates of fault dips associated with each type of surface expression. The amount of horizontal movement across a thrust fault can be determined from the measured displacement of features on either side, most usefully offset crater rims (Galluzzi et al., 2015). The steeper the average fault dip, the less horizontal movement is accommodated by each fault of a given horizontal offset, and so the lower the amount of global contraction necessary to account for it. The derived reduction in global radius recorded by Mercury's crust is 7.1 km if the average fault dip is 25°, but as little as 4.7 km if the average fault dip is 35° (Byrne et al., 2014). Watters (2021) uses a more conservative number of faults on Mercury to claim a maximum global contraction of only 1–2 km, but this too is based on average fault dips of 25°–35°. Thus, an understanding of the average dip of the faults on Mercury is vital to constrain contraction estimates and

* Corresponding author.
E-mail address: david.l.pegg@open.ac.uk (D.L. Pegg).

https://doi.org/10.1016/j.pss.2021.105223
Received 11 September 2020; Received in revised form 12 March 2021; Accepted 29 March 2021
Available online 1 April 2021

therefore to understand Mercury's thermal history. Estimates of fault dips range between 6° and 57° with an average of 25° (Galluzzi et al., 2015, 2019) were made using the shortening and vertical offset of craters that straddle faults on lobate scarps. Crane (2020) used topographic data and modelling to estimate a dip for 29 faults; all results being less than 20°, with average dips ranging from 3° to 10°. Until now no fault dip on Mercury has been measured by direct means.

2. A fault's dip revealed

Here we describe the first reported example on Mercury where the local topography exposes a fault scarp sufficiently well that its dip of the

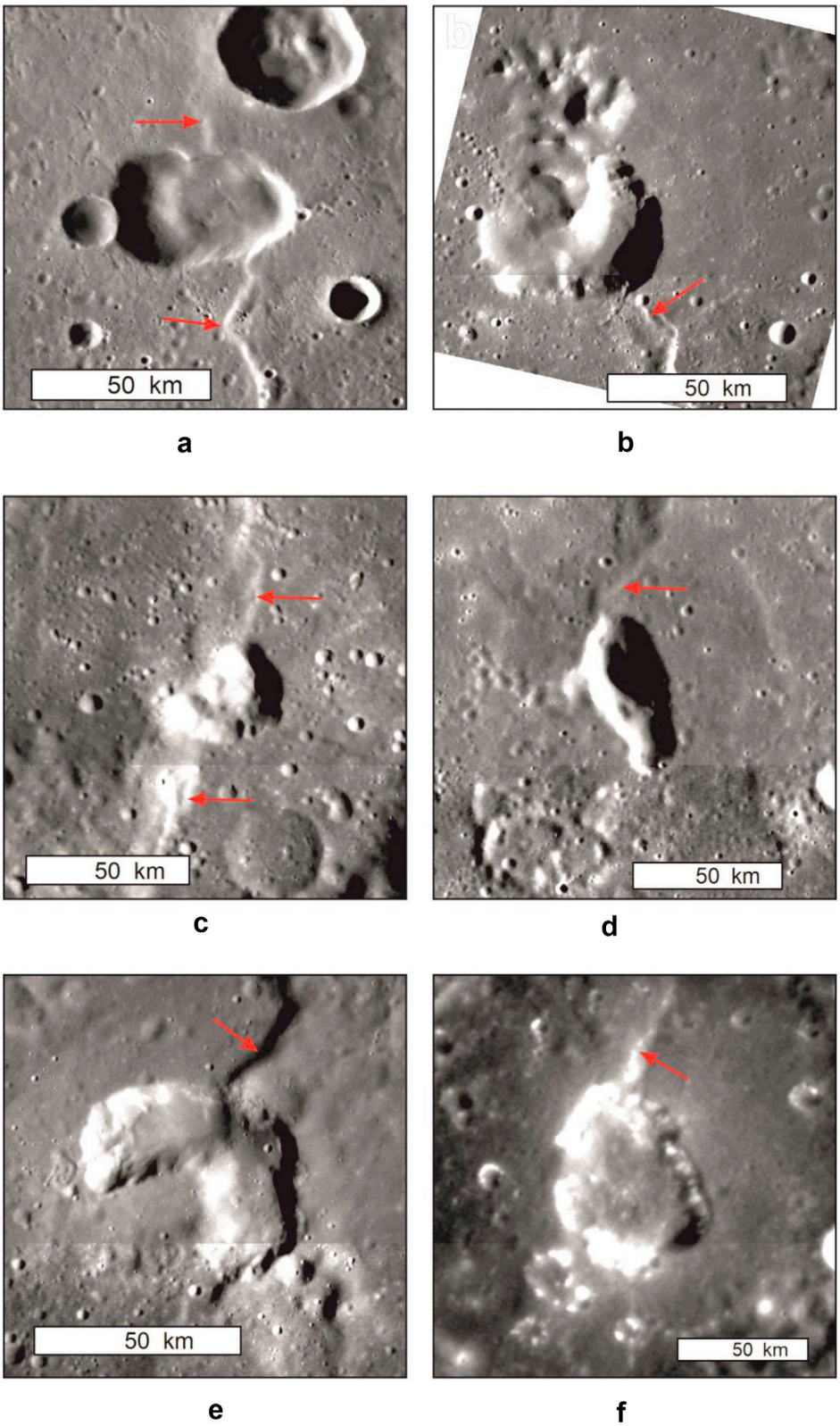

Fig. 1. Selection of volcanic vents that are coincident with contractional structures, but which do not adequately reveal the fault geometry. Red arrows point to scarps. a: image: EN1014936140M, centre: 148°E, 24°N. b: image: EN1048654092M centre: 67°W, 21°N. c: image: EN1021068336M centre: 105°W, 24°N. d: image: EN0258310462M centre: 162°W, 17°S. e: image: EN0257073440M centre: 112° W, 15°N. f: image: EN0131771793M centre: 30° E. 27°N. Alone among these, example (a) is the only one where the available images contain hints about fault dip within the vent (towards the east in that case), but no image with sufficient resolution, shadows, or stereo pair is available to measure it.

fault plane can be measured. Our example comes from the inner wall of a pit interpreted as an explosive volcanic vent.

Explosive volcanism is manifest on Mercury through endogenic pits (vents) that are up to tens of kilometres across and several kilometres deep. The vents are often surrounded by faculae: high albedo, spectrally red features that are probably explosive ejecta from the eruptions (Head et al., 2008; Goudge et al., 2014). Unlike impact craters, these vents tend to be non-circular and lack a raised rim, and hence we refer to the break of slope at the edge of a pit as the 'brink' to avoid confusion with the rim of an impact crater. High-resolution studies of these vents suggest that they did not form through caldera collapse (Rothery et al., 2014; Thomas et al., 2014b), in which the emptying of a magma chamber leads to subsidence creating a large volcanic crater. Instead, the vents are interpreted to be excavated by explosive eruption, perhaps analogous to kimberlite pipes on Earth (White and Ross, 2011).

Explosive volcanism peaked during Mercury's Calorian (3.9–~3.5–3.0 Ga) and Mansurian (~3.5–3.0 to ~1.0–0.28 Ga) epochs but continued into the Kuiperian (Thomas et al., 2014a; Jozwiak et al., 2018), which may have begun as recently as 280 Ma (Banks et al., 2017). As Mercury's lithosphere has cooled, it has thickened (Peplowski et al., 2011), and contraction hinders volcanism by impeding magma ascent (Solomon, 1978). The formation of volcanic vents on Mercury therefore probably requires crustal weakness to aid continued rising of the magmas (Klimczak et al., 2018), which are generally presumed to be volatile-rich to account for the explosivity of these eruptions (e.g. Kerber et al., 2009; Weider et al., 2016). Possible crustal weaknesses include fractures associated with impact craters, and faulting. Vents are found both within impact craters and on lobate scarps (Thomas et al., 2014b; Goudge et al., 2014). There is a significant correlation between impact craters and vents, but the high density of tectonic features on Mercury means it is not

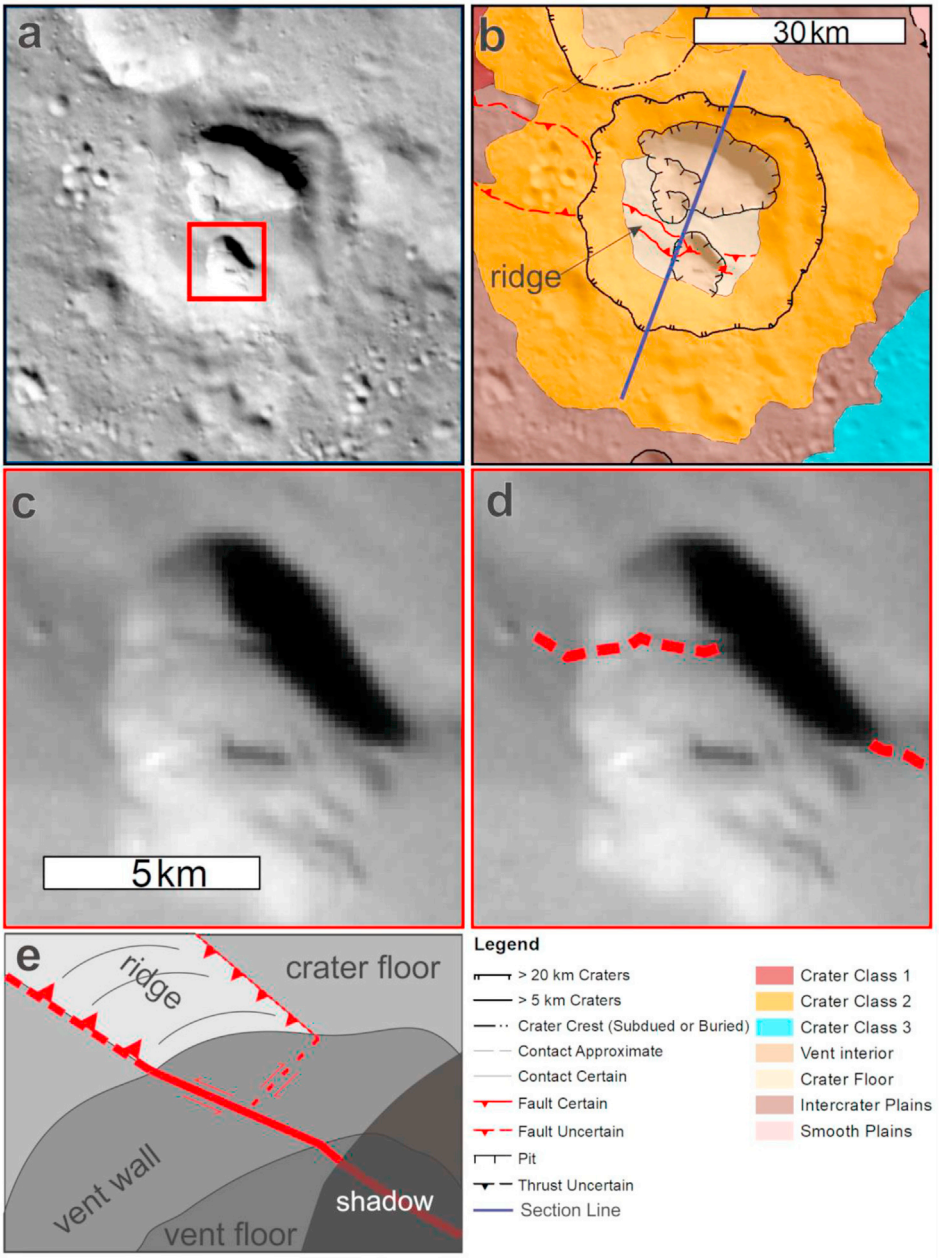

Fig. 2. a: Image EN0261054374M, showing the location of panels c and d. (red box) Image centre:147°E −65.5°N. b: interpreted geological map of area in a. showing vents and fault location and section line (purple) and label of ridge on crater floor between the two possible faults. c: Close up of vent within which the fault trace is visible. d: same area as c. with fault trace measured highlighted in red. e. illustrative diagram looking northwest showing the view of the crater floor, ridge and fault.

possible to distinguish from random whether there are also tectonic controls on the locations of vents (Klimczak et al., 2018).

During the process of reviewing volcanic vents on Mercury (Pegg et al., 2020) we identified several vents that occur directly on a tectonic fault (Fig. 1). The fault scarp is not usually visible within such vents. There are many factors that could contribute to this, such as: the vent post-dating the fault movement, space weathering, volcanic activity or rockfalls covering the scarp, poor illumination and/or low image resolution, lack of shadows or stereo pairs. However we have identified one vent within Vazov crater (147.6°E, −65.6° N) that shows what we interpret as a small fault scarp visible beyond the north side of the vent and expressed also on the internal vent wall and on the vent floor (Fig. 2). This situation enables us to reconstruct the geometry of the fault plane from the fault's intersection with the topographic surface.

Outside of the vent on the crater floor there is a contractional ridge 3 km wide, 30 km long, which strikes NW-SW. The topographic feature continues as a ridge NW of the crater. Because it is expressed by a symmetrical ridge, the facing direction of the fault would be uncertain if that were the only evidence, but fortunately in this case the scarp of the NE dipping fault is apparent inside the vent. The section revealed in the vent wall shows that the main fault dips north. The fault trace is visible on the west wall of the vent but is hidden by the vent-wall shadow in the bottom and east of the vent (Fig. 2a, c).

3. Geological setting

To study the fault, we used images from the Narrow-Angle Camera (NAC) onboard MErcury Surface, Space ENvironment, GEochemistry, and Ranging (MESSENGER) spacecraft (Solomon et al., 2001). The vent's location in the southern hemisphere means no laser altimeter data are available. We processed the image data using the USGS's Integrated Software for Imagers and Spectrometers (v 3.5.1.7995) and produced a geologic map of the vent site based on image EN0231657081M (resolution of 163 m/pixel) using ESRI's ArcGIS software. We chose a sinusoidal projection centred on the vent. We used the mapping methods and units outlined by (Galluzzi et al., 2016) following USGS (Tanaka et al., 2011) and Planmap (Rothery et al., 2018) guidelines and classified crater degradation state using (Kinczyk et al., 2020).

The geological map (Fig. 2) and image data show that the faulted vent is one of several vents within and around a degraded impact crater. Beyond the vent, on the crater floor, the fault is clearly marked by the SW side of a 4 km wide ridge. A slope on the north side of the ridge, may represent an antithetic fault on the hanging wall (Fig. 3), as is common in reverse faulting, and indeed is possibly the case with high relief ridges on Mercury (Strom et al., 1975). Within the vent itself the main fault is clearly visible where it cuts obliquely down the western internal wall of the vent and across its floor, but the antithetic fault is hard to make out. In the east of the vent, the location of the fault rupture is in shadow, and

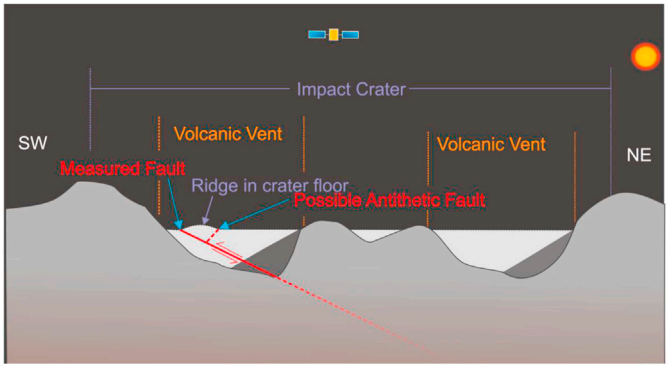

Fig. 3. Illustrative cross-section of faulted vent site, not to scale.

cannot be discerned, even by increasing the image 'stretch', but it does appear to re-emerge onto the impact crater floor east of the vent. The fault structure appears to continue beyond the vent-hosting impact crater to the northwest but is less apparent there than within the crater.

The presence of the vent within the impact crater shows that the vent postdates the formation of the impact crater. The crater degradation state corresponds to the 'partly-degraded' C2 class of the Kinczyk et al. (2020), suggesting that it formed during the Tolstojan period (~3.9–4.0 Ga); however, we could not perform a reliable crater size-frequency analysis due to the small area involved. The fault cuts across the floor of the crater, showing that it was active after the crater was formed (though could have existed before).

The timing of activity on the fault relative to the vent is also unclear. The continuity along strike of the fault on both sides of the vent might suggest the fault formed before the vent, in which case the vent-forming eruption could then have exploited the fault structure as a weakness enabling it to reach the surface, though the presence of other vents in the same crater shows this is not essential. The visibility of the fault trace on the vent wall allows us to measure the fault plane, as a result of its present-day topographic expression inside the vent wall. This could have formed during the excavation of the vent, with the excavation occurring preferentially within the fractured rock in the fault surface, leaving some of the hanging wall behind and forming a slight step. Other possible interpretations are that there has been post-eruption movement on a pre-existing fault to produce the step, or that the fault could have been initiated entirely after the vent formation.

4. Measuring the fault dip

We produced a digital terrain model (DTM) for the vent site using the AMES stereo pipeline (Broxton and Edwards, 2008) using images: EN0231657081M and EN0231356027M. We could not provide vertical control for this DTM due to the lack of laser altimeter data, so we could not eliminate the possibility that systematic tilts related to uncertainties in the spacecraft pointing remained in these data. Thus, we did not use these data to perform dip measurements. Instead, we used shadow measurements on images EN0246250635M (176 m/pixel) and EN0261431434M (197 m/pixel). These are the highest resolution close to nadir images of this feature that MESSENGER obtained. Although we examined off-nadir images as well, we elected not to attempt to use these via the method of Barnouin et al. (2012) as we would have had to correct both the shadow and horizontal measurements, and this would likely compound any errors from any uncertainty in spacecraft pointing.

As shown in Fig. 4, we constructed a line propagating the fault strike from the NW over the vent. Then we produced a second line (x) orthogonal to the strike to where the shadow from the vent intersects the fault trace. Finally, we constructed a line to record the length of the shadow from the intersection of the fault trace with the vent shadow, to the brink of the vent. We drew this line orthogonal to the shadow to get the shadow length at the point where the shadow intersects the fault trace. The incidence angle could then be used to calculate the depth of the shadow (and thus the depth of the fault trace) below the vent brink at this point (ΔZ). This could then be combined with x to get the dip angle.

For each image we repeated the measurements ten times to reduce measurement uncertainty from digitisation. We calculated the depth of vent at the intersection of the fault and the shadow using basic shadow measurement techniques e.g. (Pike, 1974; Chappelow and Sharpton, 2002) and then calculated the dip. Unfortunately, there are no markers that enable us to estimate the amount of displacement on the fault.

Our estimates for the fault plane dip from the two images are shown in a box and whisker plot (Fig. 5). The means for the two images suggests a mean dip of 28° ±5°. Uncertainties associated with this method arise from (i) possible uncertainties in spacecraft pointing, (ii) measurement error, and (iii) image resolution limits. As a test of the pointing issues, we used two nadir images to make measurements, the comparison between two images acquired at different times allowing us to test whether there

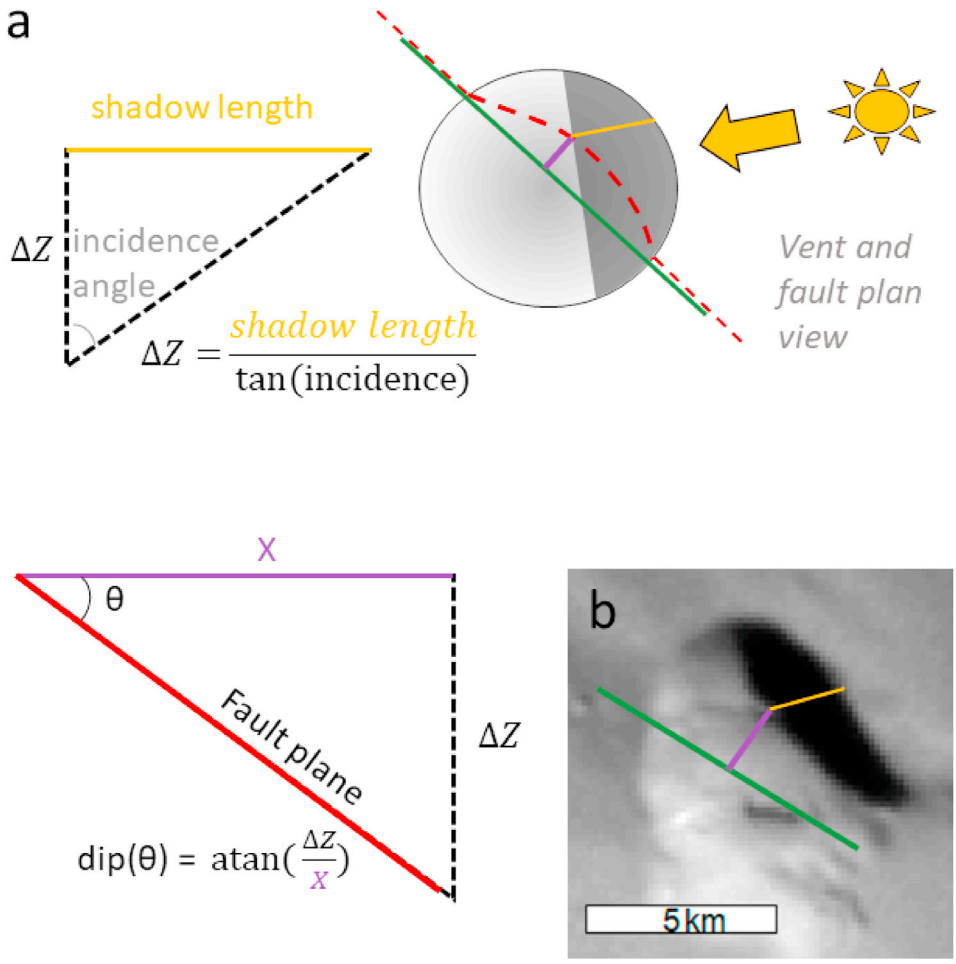

Fig. 4. a. Method for calculating dip of fault. Red: fault trace, Green line: propagated strike, Purple line: horizontal distance between strike and intersection of fault with shadow, yellow line shadow-length measurement. example of these measurements applied to image EN0261431434M.

was a pointing error offset. The dip measured in EN0246250635M has a mean of 27.8°, and median of 27.4°. The dip measured in EN0261431434M has a mean of 27.7° and a median of 27.5°. The similarity of the two measurements provides confidence in the technique. By making multiple repeat measurements we tested the repeatability of human operators to make the measurement and interpret the location of the strike and shadow intersection. This provides a measurement of the measurement error. In addition, we consider that no line can be drawn more accurately than 1-pixel width. A 1-pixel error would result in the equivalent of +5.0/-4.7° error in dip for image EN0246250635M and +5.4/-5.0° error in dip for EN0261431434M, (Fig. 5).

5. Discussion

With a dip of 28° ± 5°, this fault is slightly steeper than the mean value used by Galluzzi et al. (2019, 2015), but within the range of measured dips in their database. The upper end of the error for the dip measurement is consistent with the 30° predicted to be typical by the Anderson faulting model for a standard thrust fault (Anderson, 1905).

The scale of this fault is much smaller than that of Mercury's most characteristic lobate scarps and its surface expression is similar to high relief ridges end members of the lobate scarp – high relief ridge continuum, and its dip suggests that it is a similar compressive feature to those larger examples. This dip measurement is greater than the 3–10° estimated by Crane (2020), however those are based on features within Smooth Plains units, which are likely layered (Denevi et al., 2009) and so prone to shallow décollements (Crane and Klimczak, 2019) that would tend to encourage gentler dipping structures. The dips of faults are known on parts of Mercury to be affected by local geochemical conditions (Galluzzi et al., 2019), however the location of this faulted vent in the southern hemisphere means the geochemical data from MESSENGER is to low resolution to make inferences (Nittler et al., 2020).

While measurement of a single fault is not conclusive, our data does lend credence to the view that, on Mercury, moderately dipping faults are more typical than steeper or very shallow ones. Additionally, this work demonstrates that measurements such as these are possible and can be made even in the absence of DEM data. The image resolution does not allow measurement of fault displacement, which would enable quantification of how much strain the fault has accommodated, but higher-resolution imaging data from BepiColombo (Rothery et al., 2020) may allow this. BepiColombo should provide sufficient data to make more measurements like this, for example in occurrences such as the example in Fig. 1a, generating a database of the fault geometries in locations across Mercury and allowing a more detailed assessment of global tectonic and thermal models. If measurements of other faults prove possible and are in line with this example, generalizing such a result to the model of Byrne et al. (2014) would suggest that global contraction is likely to be about 5.7–7.1 km, which at the higher end of the currently estimated range.

6. Conclusions

Direct measurements of the dip of a fault on Mercury find a value of ~28° ± 5. This is within the range of fault dips calculated indirectly through measurements of crater displacement and for classical thrust fault models. Although only a single example, this dip estimate agrees

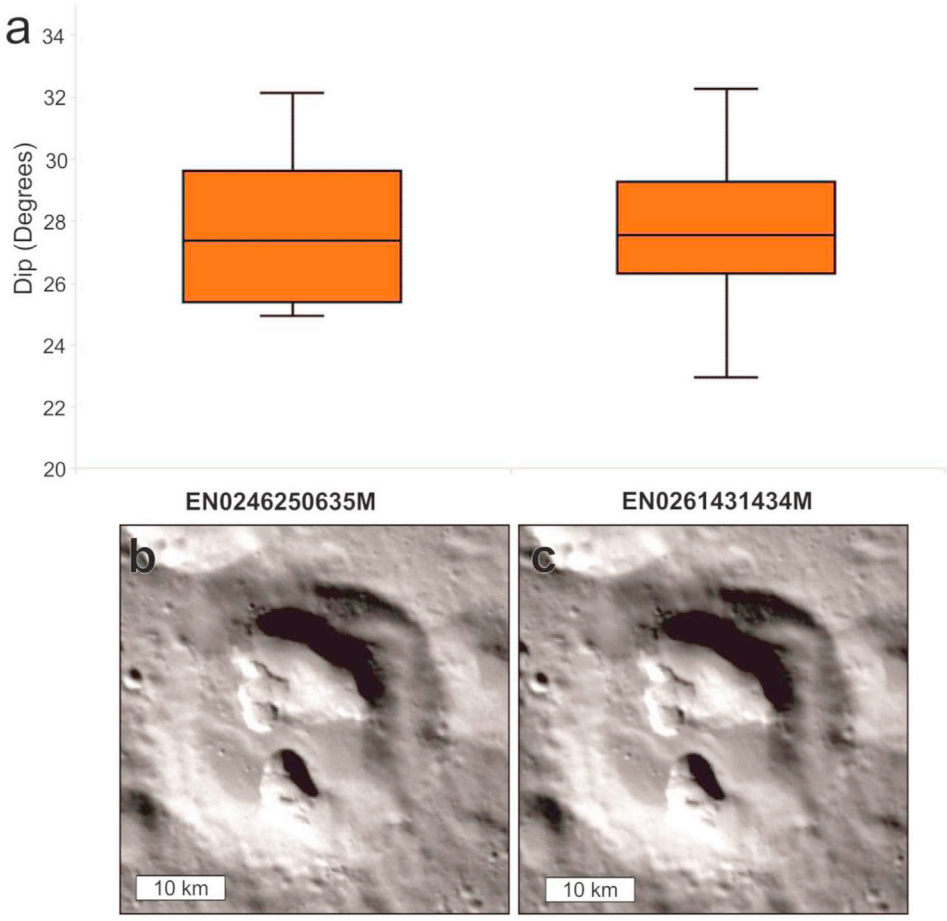

Fig. 5. a) Box and whisker plot of dip measurements on each images, each image has 10 data point and the vertical lines shows the range of data, the box encapsulates the first and third quartile with the central horizontal line the median. b) Image EN0246250635M (c) Image EN0261431434M.

with the growing evidence to suggests that the higher-end estimates of radial shrinking by global contraction are more representative than lower estimates. BepiColombo will provide an opportunity to gain better data on this site and identify other locations where the volcanic vents expose fault surfaces in 3 dimensions, offering fuller insight into planetary tectonics.

Author Statement

The research was undertaken primarily by David Pegg who first identified the feature and made the measurement and wrote the paper. Professor David Rothery, Dr Susan Conway, and Professor Matthew Balme supervised the project and provided input into developing the methodology and review & editing the paper.

Declaration of competing interest

The authors declare that they have no known competing financial interests or personal relationships that could have appeared to influence the work reported in this paper.

Acknowledgements, Samples, and Data

The image data products used in this paper are publicly available from the Planetary Data System (PDS). MESSENGER data credited to NASA/Johns Hopkins University Applied Physics Laboratory/Carnegie Institute of Washington. The geological map polygons and the calculations are avaliable here: https://ordo.open.ac.uk/collections/A_Fault_Surface_Exposed_on_Mercury/5361944; https://doi.org/10.21954/ou.rd.c.5361944.v1. David Pegg was funded by the UK Science and Technology Facilities Council (STFC) under grant ST/R504993/1, and the Open University's Space Research Area. DAR and MJB receive support from European Commission Grant 776276 (Planmap) for Mercury mapping. SJC is grateful for financial support from the French Space Agency CNES for her BepiColombo work. The authors declare no conflicts of interest and live in a relatively tectonically and volcanically boring part of one of the more active planets in the Solar System. The authors would like to thank Valentina Galluzzi and one anonymous reviewer for their input.

References

Anderson, E.M., 1905. The dynamics of faulting. Trans. Edinb. Geol. Soc. 8 (3), 387–402. https://doi.org/10.1144/transed.8.3.387.

Banks, M.E., Xiao, Z., Braden, S.E., Barlow, N.G., Chapman, C.R, Fassett, C.I, Marchi, S.S, 2017. Revised constraints on absolute age limits for Mercury's Kuiperian and Mansurian stratigraphic systems. J. Geophys. Res. Planets 122 (5), 1010–1020. https://doi.org/10.1002/2016JE005254.

Barnouin, O.S., Zuber, M.T., Smith, D.E., Neumann, G.A., et al., 2012. The morphology of craters on Mercury: results from MESSENGER flybys. Icarus 219 (1), 414–427. https://doi.org/10.1016/j.icarus.2012.02.029. Available from.

Broxton, M.J., Edwards, L.J., 2008. The Ames Stereo Pipeline: Automated 3D Surface Reconstruction from Orbital Imagery. In: , 39. Lunar and Planetary Science Conference, p. #2419.

Byrne, P.K., Klimczak, C., Celâl Şengör, A.M., Solomon, S.C., et al., 2014. Mercury's global contraction much greater than earlier estimates. Nat. Geosci. 7 (4), 301–307. https://doi.org/10.1038/ngeo2097.

Chappelow, J.E., Sharpton, V.L., 2002. An improved shadow measurement technique for constraining the morphometry of simple impact craters. Meteoritics Planet Sci. 37 (4), 479–486. https://doi.org/10.1111/j.1945-5100.2002.tb00834.x.

Crane, K., 2020. Structural interpretation of thrust fault-related landforms on Mercury using Earth analogue fault models. Geomorphology 369, 107366. https://doi.org/10.1016/j.geomorph.2020.107366.

Crane, K.T., Klimczak, C., 2019. Tectonic patterns of shortening landforms in Mercury's northern smooth plains. Icarus 317 (December 2017), 66–80. https://doi.org/10.1016/j.icarus.2018.05.034.

Denevi, B.W., Robinson, M.S., Solomon, S.C., Murchie, S.L., Blewett, D.T, Domingue, D.L, et al., 2009. The evolution of Mercury's crust: a global perspective from MESSENGER. Science 324 (5927), 613–618. https://doi.org/10.1126/science.1172226.

Dzurisin, D., 1978. The tectonic and volcanic history of mercury as inferred from studies of scarps, ridges, troughs, and other lineaments. J. Geophys. Res.: Solid Earth 83 (B10), 4883–4906. https://doi.org/10.1029/JB083iB10p04883.

Fegan, E.R., Rothery, D.A., Marchi, S., Massironi, M., et al., 2017. Late movement of basin-edge lobate scarps on Mercury. Icarus 288, 226–234. https://doi.org/10.1016/j.icarus.2017.01.005.

Galluzzi, V., Achille, G.D.I., Ferranti, L., Popa, C., et al., 2015. Faulted Craters as Indicators for Thrust Motions on Mercury, vol. 401. Geological Society, London, Special Publications, London, pp. 313–325 doi: 10.1144/SP401.17.

Galluzzi, V., Ferranti, L., Massironi, M., Giacomini, L., et al., 2019. Structural Analysis of the Victoria Quadrangle Fault Systems on Mercury: Timing, Geometries, Kinematics and Relationship with the high-Mg Region. J. Geophys. Res. 124, 2543–2562. https://doi.org/10.1029/2019JE005953, 10th ed.

Galluzzi, V., Guzzetta, L., Ferranti, L., Di Achille, G., et al., 2016. Geology of the Victoria quadrangle (H02), Mercury. J. Maps 12 (1), 227–238. https://doi.org/10.1080/17445647.2016.1193777.

Goudge, T.A., Head, J.W., Kerber, L., Blewett, D.T., et al., 2014. Global inventory and characterization of pyroclastic deposits on Mercury: new insights into pyroclastic activity from MESSENGER orbital data. J. Geophys. Res.: Planets 119 (3), 635–658. https://doi.org/10.1002/2013JE004480.

Grott, M., Breuer, D., Laneuville, M., 2011. Thermo-chemical evolution and global contraction of Mercury. Earth Planet Sci. Lett. 307 (1–2), 135–146. https://doi.org/10.1016/j.epsl.2011.04.040.

Head, J.W., Murchie, S.L., Prockter, L.M., Robinson, M.S., et al., 2008. Volcanism on Mercury: evidence from the first MESSENGER flyby. Science 321 (5885), 69–72. https://doi.org/10.1126/science.1159256.

Head, J.W., Murchie, S.L., Prockter, L.M., Solomon, S.C., et al., 2009. Volcanism on Mercury: evidence from the first MESSENGER flyby for extrusive and explosive activity and the volcanic origin of plains. Earth Planet Sci. Lett. 285 (3–4), 227–242. https://doi.org/10.1016/j.epsl.2009.03.007.

Jozwiak, L.M., Head, J.W., Wilson, L., 2018. Explosive volcanism on Mercury: analysis of vent and deposit morphology and modes of eruption. Icarus 302, 191–212. https://doi.org/10.1016/j.icarus.2017.11.011.

Kerber, L., Head, J.W., Solomon, S.C., Murchie, S.L., et al., 2009. Explosive volcanic eruptions on Mercury: eruption conditions, magma volatile content, and implications for interior volatile abundances. Earth Planet Sci. Lett. 285 (3–4), 263–271. https://doi.org/10.1016/j.epsl.2009.04.037.

Kinczyk, M.J., Prockter, L.M., Byrne, P.K., Susorney, H.C.M., et al., 2020. A morphological evaluation of crater degradation on Mercury: revisiting crater classification with MESSENGER data. Icarus 341 (January), 113637. https://doi.org/10.1016/j.icarus.2020.113637.

King, S.D., 2008. Pattern of lobate scarps on Mercury's surface reproduced by a model of mantle convection. Nature Geoscience. [Online] 1 (4), 229–232. https://doi.org/10.1038/ngeo152.

Klimczak, C., Byrne, P.K., Solomon, S.C., 2015. A rock-mechanical assessment of Mercury's global tectonic fabric. Earth Planet Sci. Lett. 416, 82–90. https://doi.org/10.1016/j.epsl.2015.02.003.

Klimczak, C., Crane, K.T., Habermann, M.A., Byrne, P.K., 2018. The spatial distribution of Mercury's pyroclastic activity and the relation to lithospheric weaknesses. Icarus 315, 115–123. https://doi.org/10.1016/j.icarus.2018.06.020.

Korteniemi, Jarmo, Walsh, Lisa S., Hughes, Scott S., 2015. Wrinkle Ridge. In: Hargitai, Henrik, Kereszturi, A. (Eds.), Encyclopedia of Planetary Landforms, pp. 2356–2364. https://doi.org/10.1007/978-1-4614-3134-3_572. Springer Reference.

Massironi, M., Byrne, P.K., 2015. High-relief ridge. Encyclopedia of planetary landforms 932–934.

Massironi, M., Byrne, P.K., Van Der Bogert, C.H., 2015. Lobate scarp. Encyclopedia of planetary landforms 1255–1262.

Matsuyama, I., Nimmo, F., 2009. Gravity and tectonic patterns of Mercury: effect of tidal deformation, spin-orbit resonance, nonzero eccentricity, despinning, and reorientation. J. Geophys. Res.: Planets 114 (1), 1–23. https://doi.org/10.1029/2008JE003252.

Melosh, H.J., Dzurisin, D., 1978. Mercurian global tectonics: a consequence of tidal despinning? Icarus 35 (2), 227–236. https://doi.org/10.1016/0019-1035(78)90007-6.

Melosh, H.J., McKinnon, W.B., 1988. The tectonics of Mercury, pp. 374–400. Mercury, 1988merc.book..374M.

Neuendorf, K.K.E., Mehl, J.P., Jackson, J.A., 2005. In: Includes Bibliographical References. *Glossary Of Geology*, fifth ed. American Geological Institute, Alexandria, Va.

Nittler, L.R., Frank, E.A., Weider, S.Z., Crapster-Pregont, E., et al., 2020. Global major-element maps of Mercury from four years of MESSENGER X-Ray Spectrometer observations. Icarus 345 (December 2019), 113716. https://doi.org/10.1016/j.icarus.2020.113716.

Pegg, D.L., Rothery, D.A., Balme, M.R., Conway, S.J., 2020. Common place multiple volcanic erruptions on mercury and their implications. In: British Planetary Science Conference. 2020. Oxford, p. 95.

Peplowski, P.N., Evans, L.G., Hauck, S.A., McCoy, T.J., et al., 2011. Radioactive Elements on Mercury's Surface from MESSENGER: Implications for the Planet's Formation and Evolution. Science 333, 1850–1852. https://doi.org/10.1126/science.1211576, 6051st, ed.

Pike, R.J., 1974. Depth/diameter relations of fresh lunar craters: revision from spacecraft data. Geophys. Res. Lett. 1 (7), 291–294. https://doi.org/10.1029/GL001i007p00291.

Rothery, D.A., Altieri, F., Balme, M.R., Carli, C., Le Mouelic, S., Mangold, N., Massironi, M., Penasa, L., Pozzobon, R, Pio Rossi, A, Van Der Bogert, C.H., 2018. Planmap Mapping Standards Document. PlanMap. Available from: https://wiki.planmap.eu/display/public/Deliverables?preview=/8193472/8193931/776276-planmap_D2.1.pdf.

Rothery, D.A., Massironi, M., Alemanno, G., Barraud, O., et al., 2020. Rationale for BepiColombo studies of Mercury's surface and composition. Space Sci. Rev. 216 (4), 66. https://doi.org/10.1007/s11214-020-00694-7.

Rothery, D.A., Thomas, R.J., Kerber, L., 2014. Prolonged eruptive history of a compound volcano on Mercury: volcanic and tectonic implications. Earth and Planetary Science Letters 385, 59–67. https://doi.org/10.1016/j.epsl.2013.10.023.

Solomon, S.C., 1978. On volcanism and thermal tectonics on one-plate planets. Geophys. Res. Lett. 5 (6), 461–464. https://doi.org/10.1029/GL005i006p00461.

Solomon, S.C., 1977. The relationship between crustal tectonics and internal evolution in the moon and Mercury. Phys. Earth Planet. In. 15 (2–3), 135–145. https://doi.org/10.1016/0031-9201(77)90026-7.

Solomon, S.C., McNutt Jr., R.L., Gold, R.E., Acuña, M.H., et al., 2001. The MESSENGER mission to Mercury : scientfic objectives and implementation. Planet. Space Sci. 49, 1445–1465. https://doi.org/10.1016/S0032-0633(01)00085-X.

Strom, R.G., Trask, N.J., Guest, J.E., 1975. Tectonism and volcanism on mercury. J. Geophys. Res. 80 (17), 2478–2507. https://doi.org/10.1029/JB080i017p02478.

Tanaka, K.L., Skinner, J.A., Hare, T.M., 2011. Planetary Geologic Mapping Handbook – 2011. *Abstracts Of the Annual Meeting Of Planetary Geologic Mappers*. U.S. Geological Survey, Astrogeology Science Center, p. 21. https://ntrs.nasa.gov/archive/nasa/casi.ntrs.nasa.gov/20100017213.pdf.

Thomas, R.J., Rothery, D.A., Conway, S.J., Anand, M., 2014a. Long-lived explosive volcanism on Mercury. Geophysical Research Letters. [Online] 41 (17), 6084–6092. https://doi.org/10.1002/2014GL061224.

Thomas, R.J., Rothery, D.A., Conway, S.J., Anand, M., 2014b. Mechanisms of explosive volcanism on Mercury: implications from its global distribution and morphology. *J. Geophys. Res.: Planets*. [Online] 119 (10), 2239–2254. https://doi.org/10.1002/2014JE004692.

Watters, T.R., 2021. A case for limited global contraction of Mercury. Commun. Earth Environ. 2 (1), 1–9. https://doi.org/10.1038/s43247-020-00076-5.

Watters, T.R., Nimmo, F., 2010. The tectonics of Mercury. In: Planetary Tectonics. Cambridge University Press, pp. 15–80.

Watters, T.R., Selvans, M.M., Banks, M.E., Hauck, S.A., et al., 2015. Distribution of large-scale contractional tectonic landforms on Mercury: implications for the origin of global stresses. Geophys. Res. Lett. 42 (10), 3755–3763. https://doi.org/10.1002/2015GL063570.

Watters, T.R., Solomon, S.C., Robinson, M.S., Head, J.W., et al., 2009. The tectonics of Mercury: the view after MESSENGER's first flyby. Earth Planet Sci. Lett. 285 (3–4), 283–296. https://doi.org/10.1016/j.epsl.2009.01.025.

Weider, S.Z., Nittler, L.R., Murchie, S.L., Peplowski, P.N., et al., 2016. Evidence from MESSENGER for sulfur- and carbon-driven explosive volcanism on Mercury. Geophys. Res. Lett. 43 (8), 3653–3661. https://doi.org/10.1002/2016GL068325.

White, J.D.L., Ross, P., 2011. Maar-diatreme volcanoes: a review. J. Volcanol. Geoth. Res. 201 (1–4), 1–29. https://doi.org/10.1016/j.jvolgeores.2011.01.010.